



Cite this: *Phys. Chem. Chem. Phys.*,
2015, 17, 8758

Local structure and dynamics of lithium garnet ionic conductors: tetragonal and cubic $\text{Li}_7\text{La}_3\text{Zr}_2\text{O}_{12}$

Matthew Klenk and Wei Lai*

To better understand the ionic conduction in lithium garnet oxides, we employed molecular dynamics simulation to investigate the local structure and dynamics of a model material $\text{Li}_7\text{La}_3\text{Zr}_2\text{O}_{12}$ and origin of its tetragonal to cubic phase transition. Our simulations were able to produce lattice parameter, neutron scattering, and conductivity data close to those gathered using experimental techniques, which allows us to study atomic-scale details of this complex material. First, it was found that lithium atoms primarily perform oscillation and "structured diffusion" dynamics in the tetragonal and cubic phase, respectively. Second, we believe that the tetragonal to cubic phase transition is an entropy-driven one that involves redistribution of lithium atoms among all tetrahedral sites. The transition is likely to initiate on the tetrahedral 8a site but needs the cooperation of neighboring octahedral 32g Li as relay atoms. Finally, it was found that a few types of lithium clusters dominate in both phases of $\text{Li}_7\text{La}_3\text{Zr}_2\text{O}_{12}$, which leads to highly correlated motion of lithium atoms. The local symmetry of these clusters dictates a "center-pass" mechanism as lithium goes through the bottleneck.

Received 5th December 2014,
Accepted 10th February 2015

DOI: 10.1039/c4cp05690f

www.rsc.org/pccp

Introduction

As the need to develop technology aimed at transitioning away from hydrocarbon-based fuels continues to increase, the development of safe high performance battery systems is of the utmost importance. Currently, solvent-based electrolytes are the most popular commercial option in lithium-ion batteries due to their high conductivity and relatively inexpensive manufacturing cost. However, these liquid systems are subject to solid electrolyte interphase (SEI) degradation through cell cycling and they incorporate volatile and flammable solvents that are prone to combustion.^{4–6} To mitigate these issues, much time and effort has been spent researching the lithium garnet oxides as a suitable solid-state electrolyte to replace these liquid systems. Lithium garnet oxides have shown to be very accommodating to various cation-doping schemes allowing the concentration of lithium in the crystal to vary from as little as three to as much as seven per formula unit, with conductivities ranging from $10^{-10} \text{ S cm}^{-1}$ to $10^{-3} \text{ S cm}^{-1}$, as summarized in a recent review paper.⁷

One of the most widely studied compositions of the lithium garnet series is the end member $\text{Li}_7\text{La}_3\text{Zr}_2\text{O}_{12}$ (Li7LZ), which

exhibits two crystalline phases, a tetragonal structure with space group $I4_1/acd$, and a cubic structure with space group $Ia\bar{3}d$.⁹ Fig. 1 presents the schematics of the representative structural units in the tetragonal phase. Lithium can occupy either the tetrahedral (Td) or octahedral (Oh) site/cage formed by the oxygen atoms (not shown). Each Td site is coordinated with four Oh cages, while each Oh site is coordinated with two Td cages. The 3D connection of these two types of cages can be better visualized if they are projected on 2D. The tetragonal phase is characterized by ordering of Li^+ between its two tetrahedral (Td) sites, the occupied Td-8a site and unoccupied Td-16e site. There are also two distinct octahedral (Oh) sites, Oh-16f and Oh-32g, both of which are fully occupied. The cubic

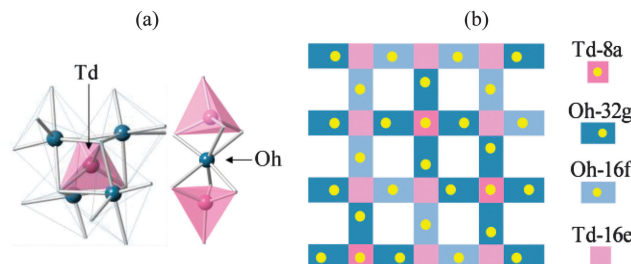


Fig. 1 Schematics of structural units in the tetragonal phase of $\text{Li}_7\text{La}_3\text{Zr}_2\text{O}_{12}$. (a) A tetrahedral (Td) site surrounded by four octahedral (Oh) cages; an Oh site surrounded by two Td cages. (b) Connectivity pattern of Td (8a and 16e) and Oh (16f and 32g) cages projected on 2D.

Chemical Engineering and Materials Science, Michigan State University, East Lansing, Michigan, USA. E-mail: laiwei@msu.edu

† Electronic supplementary information (ESI) available: Movies of atomic dynamics of four examples in Fig. 8. See DOI: 10.1039/c4cp05690f

phase of Li₇LZ as well as lower lithium concentration members of the garnet family exhibits disorder about two lithium crystallographic sites, a tetrahedral (Td-24d, *i.e.* disordered 8a and 16e) and an octahedral (Oh-48g, *i.e.* disordered 16f and 32g). The cubic phase exhibits ionic conductivity that is orders of magnitude higher than that in the tetragonal phase. However, at present it is not clear what experimental conditions would yield the cubic and tetragonal phase, respectively, as it appears that Li₇LZ is sensitive to thermal treatment, Al contamination, and H₂O/CO₂ exposure. Even for the “un-doped” Li₇LZ samples, different transition temperatures were reported for the low-temperature tetragonal to high-temperature cubic phase transition. For example, Geiger *et al.*¹⁴ Adams *et al.*,¹³ Kuhn *et al.*,¹⁶ Larraz *et al.*,³ and Matsui *et al.*⁸ reported transition temperatures of 373–423 K, 450 K, 623 K, 918 K, and 923 K, respectively, from high-temperature X-ray diffraction (XRD) or nuclear magnetic resonance (NMR) studies.

In addition to the above-mentioned experimental efforts, computational studies based on force-fields and density functional theory (DFT) have been performed to investigate the phase transition and local structure and dynamics of Li₇LZ garnet. Adams and Rao¹³ were the first to perform classical molecular dynamic (MD) on Li₇LZ with their own Morse-type force-fields. Their work presented conductivity values of cubic Li₇LZ similar to those of experimental measurements and reported a tetragonal-cubic transition temperature of 400 K. On the other hand, the transition temperature was found to be between 800 and 1000 K by first-principles molecular dynamics (FPMD) simulation based on DFT, performed by Bernstein *et al.*¹⁷ They also showed that the transition temperature decreases with increasing Li vacancy. However, there were no conductivity studies in this work. Regarding the local structure and dynamics of Li₇LZ, work presented by Xu *et al.* examined the minimum energy pathways for Li⁺ using the nudged elastic band (NEB) technique based on DFT.¹⁸ Their work proposed that lithium atoms in the cubic phase of Li₇LZ bypass the center of the 24d site and instead move along the edge of the 24d site between neighboring 48g octahedrons. This “edge-pass” mechanism was later supported by the FPMD simulations from Jalem *et al.*¹² and Miara *et al.*¹¹ In addition, Jalem *et al.*¹² showed that lithium diffusion in cubic Li₇LZ progresses through a concerted migration mechanism between neighboring lithium sites. This was confirmed by Meier *et al.*’s investigation that also showed that Li diffusion is more coordinated in tetragonal Li₇LZ than that of the cubic phase.¹⁹ However, these DFT-based studies have been using a single unit cell and FPMD simulation has been limited to tens of picoseconds, which raises the question of statistical prevalence of the observed phenomena. The present authors previously developed force-field parameters for Li_{7-x}La_xZr_{2-x}Ta_xO₁₂ composition series and studied the local structure and dynamics of another model material Li₅La₃Ta₂O₁₂ (Li₅LT).^{1,15} The objective of this paper is to employ classical MD simulation based on these force-field parameters to investigate local structure/dynamics of lithium atoms, in order to paint a more comprehensive picture of phase transition and lithium conduction in Li₇LZ garnets.

This manuscript is organized as follows. First, we demonstrate our simulation approaches are able to produce phase transition behaviors (change of lattice parameters and transition

temperatures), neutron scattering pair distribution functions (PDF), and ionic conductivities that agree well with experimental results. Second, we analyze the van Hove time-space correlation functions to obtain an overall picture of the time and spatial dependence of local structure and dynamics of lithium atoms in the tetragonal and cubic phases. Third, we examine probability density functions (p.d.f.), occupancy, and atomic mean square displacements of lithium, in order to elucidate the phase transition mechanism. Finally, we study lithium dynamics by investigating the evolution of lithium clusters and lithium motion between tetrahedral and octahedral cages, as a function of temperature.

Methods

Classical MD simulations were performed on 2 × 2 × 2 supercells (1536 atoms) of Li₇LZ using the DLPOLY Classic package.²⁰ Empirical force-fields similar to our previous work were employed which include the long-range Coulombic potential, short-range Buckingham potential, and Dick–Overhauser core-shell potential for O atoms.^{1,21} The force-field parameters are listed in Table 1. We slightly tuned the Buckingham parameters of Zr–O interaction to obtain a better match to experimental lattice parameters of Li₇LZ.¹⁶ Velocity Verlet integration with a time step of 0.25 fs was employed for all trials. Constant number, stress, and temperature ($N\sigma T$) ensemble simulations were performed for 100 ps with 0 GPa stress to obtain the lattice shape and parameters. The Berendsen thermostat and barostat with relaxation time constants of 0.05 and 0.25 ps were used respectively. The initial configuration was equilibrated at 1400 K using $N\sigma T$ dynamics to initialize the structure and simulate synthesis conditions for the lower temperature trials. Subsequent $N\sigma T$ runs were performed between 1300 K and 300 K with 100 K decrements. Upon the completion of the $N\sigma T$ simulations, average lattice parameters were extracted and used to determine the cell size for constant number, volume, and energy (NVE) dynamics. The NVE simulations were performed for 1 ns outputting atomic positions every 0.1 ps. To sample the fine details of lithium dynamics, additional NVE simulations were carried out for 2.5 ps with trajectories saved every 2.5 fs at both 300 K and 1100 K.

The analysis of atomic trajectories has been focused on the number density $\rho(r,t)$ and time-space correlation of number density as van Hove correlation functions $G(r,t)$, as discussed in the Appendix. The time-averaged number density, *i.e.* probability density function (p.d.f.) or density map, was evaluated by dividing simulation cell into pixels with roughly 0.1 Å in length.

Table 1 Force-field parameters

	Buckingham parameters			O shell parameters	
	A (eV)	ρ (Å)	C (eV Å ⁶)	Y (e)	-2.76
Zr–O	1385.02	0.3500	0	k (eV Å ⁻²)	30.2
La–O	4579.23	0.3044	0	m (au)	0.2
Li–O	632.102	0.2906	0		
O–O	22764.30	0.1490	27.63		

At each time step, we counted whether each pixel is occupied by lithium and averaged over all the time steps. The tetrahedral and octahedral cages are defined as spherical regions with radii of 0.65 and 1.40 Å centered at the tetrahedral and octahedral sites, respectively. The occupancy values of tetrahedral and octahedral cages, effectively the integration of p.d.f. over cages, were averaged over all the time steps. Mean squared displacements (MSD), which are related to $G(r,t)$, were calculated over the last 500 ps of the simulation using the definition $\langle |\delta r_i(t)|^2 \rangle = 1/N \sum_{i=1}^N \langle |r_i(t) - r_i(0)|^2 \rangle$. The self-diffusivity, $D = 1/6 \lim_{t \rightarrow \infty} \langle |\delta r_i(t)|^2 \rangle / t$ was extracted from the slope of MSD vs. time plot for the last 100 ps of our simulation. As performed in our previous work, the thermodynamic factor $\Gamma = (\partial \mu / \partial \ln N)_T, \sqrt{(k_B T)} = \langle N \rangle / \sigma_N^2$ was evaluated by averaging the fluctuation in the number of lithium ions within 1/8 and 1/10 subset of our simulation cell over the last 500 ps.^{1,22} The ionic conductivity values were calculated according the modified Nernst–Einstein relation as $\sigma = \Gamma^{-1} (z_i e)^2 D \rho / (k_B T)$, where $z_i e$ is the charge, k_B is the Boltzmann constant, T is the absolute temperature, and ρ is the nominal number density.

Results and discussion

Validation of simulation process

To demonstrate the validity of our force-field model and our simulation approaches, we compared lattice parameters, neutron scattering PDF, and ionic conductivities calculated from MD simulation with those from literatures, as shown in Fig. 2. In Fig. 2a, the lattice parameters outputted by our simulation match well with X-ray and neutron diffraction data independently collected from Wang *et al.*,¹ Awaka *et al.*,² and Larraz *et al.*³ The thermal expansion along the *a/b* directions proceeds until a temperature of 700 K is obtained, at which point the lattice contracts in those directions. The rate of thermal expansion along the *c* direction increases in a nonlinear fashion until the temperature reaches 900 K, above which Li7LZ is in the cubic phase.

When the tetragonal lattice parameters were converted to pseudo-cubic ones, a linear expansion was observed for the whole temperature range. This transition temperature of 900 K is in agreement with the reported transition temperature of 918 K by Larraz *et al.*³ using high-temperature XRD and 923 K by Matsui *et al.* using high-temperature XRD and thermal analysis.⁸ FPMF work by Bernstein *et al.*¹⁷ predicted a transition temperature between 800–1000 K but did not investigate the transition temperature to a higher resolution. This temperature of 900 K is much higher than those reported elsewhere, *e.g.* 373–423 K from Geiger *et al.*,¹⁴ 450 K from Adams *et al.*,¹³ 623 K from Kuhn *et al.*¹⁶ It is plausible that these samples were contaminated with Al, H₂O, or CO₂, which lowers the transition temperature.

In addition to lattice parameters, we employed another fingerprint function, *i.e.* neutron scattering PDF, to check if our simulations are generating reliable results. The comparison of PDF at 300 K, in the form of $G^{\text{PDF}}(r)$, from MD simulation and neutron scattering experiments is shown in Fig. 2b. Since we do not have neutron total-scattering data for Li7LZ, we calculated $G^{\text{PDF}}(r)$ based on the Rietveld refinement results of conventional neutron diffraction data from our previous work.¹ Specifically, we utilized the software package PDFGUI²³ to calculate $G^{\text{PDF}}(r)$ from the structure file of Li7LZ at 300 K, supplied as supplementary data in the literature.¹ We consider this as an “experimental” approach. Because Rietveld refinement assumes independent atomic models, it is expected that this approach will generate PDF patterns similar to those from total-scattering experiments but with variance in peak intensities and width. Such variance is due to the difference in the average structure (from the Rietveld refinement) and the local structure, as shown in the study of Bi₂O₃.²⁴ As shown in Fig. 2b, the PDF plot from MD simulation agrees well with that from the “experimental” approach, except the first two peaks. MD simulation predicts stronger peaks suggesting atomic correlation.

Finally, we looked at the ionic conductivity values at different temperatures shown in Fig. 2c. Experimental values from Matsui *et al.*⁸ and Wang *et al.*¹⁰ report a superionic transition,²⁵ where a poorly conductive phase turns into a more conducting phase

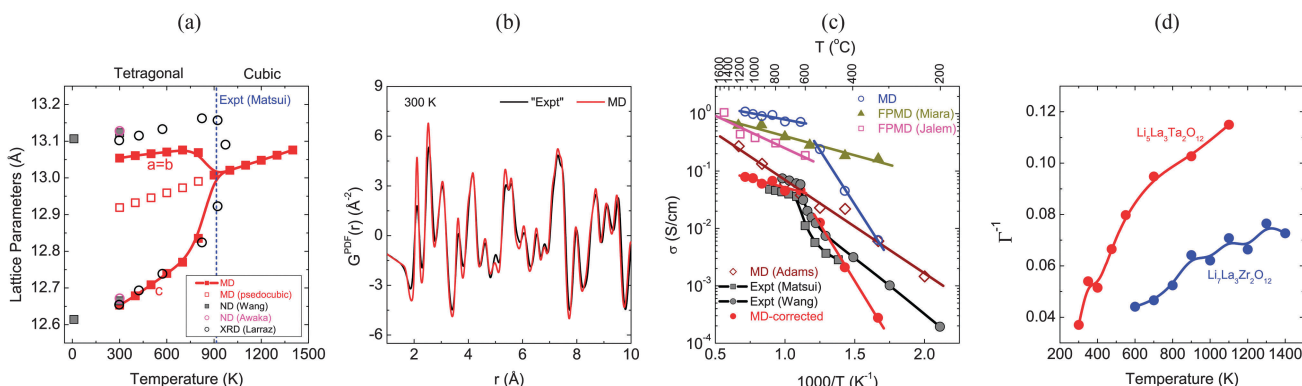


Fig. 2 Comparison of physical parameters from MD simulation and literature results. (a) Lattice parameters including experimental values of ND and XRD results from Wang *et al.*,¹ Awaka *et al.*,² Larraz *et al.*,³ and Matsui *et al.*⁸ (b) Neutron scattering PDF $G^{\text{PDF}}(r)$. (c) Ionic conductivities including experimental values from Matsui *et al.*⁸ and Wang *et al.*,¹⁰ and literature results from Miara *et al.*,¹¹ Jalem *et al.*,¹² and Adams *et al.*¹³ (d) Inverse thermodynamic factors compared to those of Li5LT from Wang *et al.*¹⁵

upon heating. The superionic transition temperature coincides with that in the lattice parameter plot. In this Fig. 2c, we reported two different methods, labeled as “MD” and “MD-corrected”, for finding the conductivity of Li₇LZ. In the “MD” plot, the Nernst–Einstein equation was applied to convert self-diffusivity to conductivity, similar to what has been previously performed in literature.^{11–13} However, the Nernst–Einstein equation is only suitable for ideal systems. In lithium garnets there is a high concentration of Li, and these atoms interact. Calculating the conductivity directly using the Nernst–Einstein equation is likely to significantly overestimate its value, as shown in the “MD” plot and two plots from literature in Fig. 2c. To correct for this, we evaluated the thermodynamic factor as described in the methods section and multiplied it to the Nernst–Einstein conductivity, *i.e.* “MD-corrected”. This approach was shown in our recent work to yield reliable conductivities for another garnet Li₅LT.¹⁵ Our present simulation results, labeled as “MD-corrected”, successfully captured the transition of Li₇LZ, although the calculated ionic conductivities in the tetragonal phase are lower than those from experiments (especially below 400 °C). It is possible that experimental samples contain more disorder than our simulation cells and this contributes to the higher conductivities. Another classical MD simulation, labeled as “Adams”, presented higher conductivities across the temperature range but predicted the transition temperature to be 400 K (not shown). This simulation also yielded Li–Li pair distribution function inconsistent with experiments, which will be discussed later.

The thermodynamic factor Γ can be used as a measure of how ideally a system is behaving. An ideal gas will have a Γ or Γ^{-1} equal to 1, while low values of Γ^{-1} observed in our simulations indicate each Li hopping event is not independent and is affected by how the other Li in the system are moving. The inverse thermodynamic factor for Li₇LZ, in Fig. 2d, is consistently lower than that of Li₅LT from our recent work.¹⁵ This is a reasonable result considering that increasing the Li concentration limits the number of ways in which Li will locally distribute themselves. This point will be discussed further in the later section regarding lithium clusters and dynamics.

It can be seen from Fig. 2 that our MD simulations have predicted physical parameters that agree well with those from experiments. In the subsequent sections, we will take a closer look at the atomic-scale details of local structure and dynamics and phase transition of Li₇LZ.

Lithium structure and dynamics: van Hove correlation functions (VHCF)

Van Hove time-space correlation functions are valuable fingerprint functions to describe atomic structure and dynamics.²⁶ For example, the self-part of van Hove correlation function (VHCF), $G_s(r,t)$ or its transformed version $4\pi r^2 G_s(r,t)$, is related to the probability of finding one atom after it travels a distance of r for a time interval of t . Such function is the natural choice to study atomic dynamics. On the other hand, the distinct-part of van Hove correlation function, $G_d(r,t)$ or its transformed version $4\pi r^2 G_d(r,t)$, is related to the probability of finding one atom when a different atom is away from this atom with a

distance of r and a time interval of t . This function is generally used to present the structure of the atoms. Although van Hove correlation functions provide the most comprehensive information on the structure and dynamics, two other types of high-level fingerprint functions are routinely employed: mean square displacements (MSD) and pair distribution function (PDF). The relation of MSD and PDF to VHCF is shown in the Appendix. The MSD function lost the spatial information by taking integrals over all r values. On the other hand, the PDF function lost the temporal information by looking at the static limit.

Fig. 3 shows (a) the self-part of VHCF as $4\pi r^2 G_s(r,t)$ of lithium atoms and (b) its projection along the space and time axis at 300 K. There is a high probability of finding lithium atoms with displacement of 0.2 Å and such probability shows weak time dependence for different displacement values (0.11, 0.23, 0.58 Å). Such correlation function is typical of atomic oscillation around equilibrium positions, which is expected for lithium atoms in the ordered tetragonal phase. Fig. 3 also shows the (c) distinct-part of the VHCF as $G_d(r,t)$ of lithium atoms and (d) its projection along the space and time axis at 300 K. The dependence on the distance is characteristic of pairs showing short-range order (peaks at small distances) but long-range disorder (oscillating around 1 at large distances). Such structure features are generally found in liquids or glasses. A small time-dependence at short time, *e.g.* 0.1 ps, was observed.

The high-level presentation of VHCF is shown in Fig. 4 as MSD and PDF plots for both 300 K and 1100 K. Again, a flat MSD plot at 300 K in Fig. 4a is a signature of oscillation. The linear MSD plot at 1100 K is a signature of diffusion that we will discuss more in Fig. 5. In Fig. 4b, we also present the Li–Li PDF plots from “experiments” and literature. Using the same approach discussed previously for the neutron scattering PDF, we calculated the “experimental” partial Li–Li PDF and we found it is similar to that from our MD simulation. Again, the slight difference is due to the difference between the average and local structure, as discussed previously. However, MD simulation by Adams *et al.* generates two peaks (2.35 and 2.8 Å), suggesting that their Morse-type force-fields may not be able to capture the real dynamics of lithium motion. With the increase of temperature from 300 to 1100 K, the first peak in the Li–Li pair becomes wider and moves to a smaller distance, indicating weaker Li–Li repulsion at higher temperatures.

Fig. 5 shows (a) the self-part of VHCF as $\log_{10} 4\pi r^2 G_s(r,t)$ of lithium atoms and (b) projection of $4\pi r^2 G_s(r,t)$ along the space and time axis at 1100 K. It is apparent that lithium atoms at this temperature can move different distances for different time intervals, as expected for a diffusion mechanism. To understand such complex time and space dependence and diffusion details, we can look at a simple model system. According to eqn (A6) in the Appendix, a linear MSD plot at 1100 K as seen in Fig. 4a is consistent with a continuous random-walk or structureless diffusion model. Based on the diffusivity extracted from Fig. 4a, we then plot the self-part of VHCF of a continuous random-walk model in Fig. 5c and d. As expected, there is one peak along the distance axis in Fig. 5d due to the competing

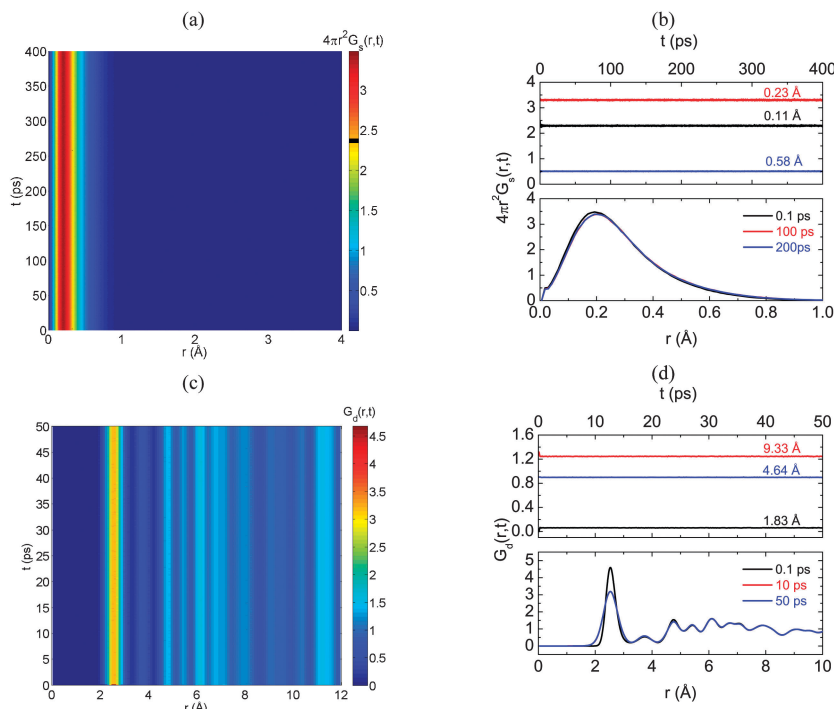


Fig. 3 (a) Self-part of the van Hove correlation function and (b) its spatial and temporal projection at 300 K. (c) Distinct-part of the van Hove correlation function and (d) its spatial and temporal projection at 300 K.

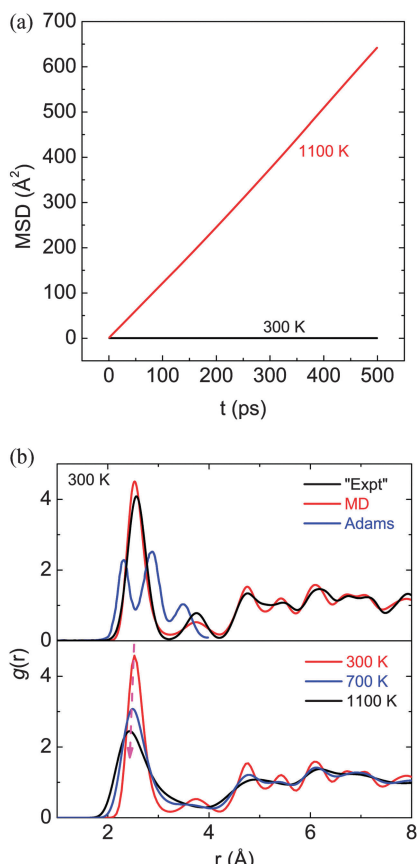


Fig. 4 (a) Mean squared displacement (MSD) of Li at 300 K and 1100 K. (b) Partial pair distribution function of Li–Li pairs at different temperatures. Literature results from Adams *et al.*¹³ are included.

quadratic and exponential term in eqn (A5) in the Appendix. Similarly, there is one peak along the time axis due to the competing power and exponential term in eqn (A6). In Fig. 5c, such dependence shows up as “expanding galaxies”. When we compare Fig. 5b and d, it is clear that selected projection plots at different spatial and temporal values in Fig. 5b deviate from this continuous random-walk model. For example, several peaks along the distance axis were observed and this leads to “mountain-like” features in the overall VHCF plot in Fig. 5a. When we compare Fig. 3a, 5a and c, we can propose that diffusion behaviors at 1100 K, *i.e.* Fig. 5a, are intermediate between an oscillation type and continuous random-walk type, which we will call as “structured diffusion”. This has generally been called a local jump mechanism when quasielastic neutron scattering (QENS) experiments were used to study atomic diffusion in materials. Several models, *e.g.* Chudley–Elliott,²⁷ Hall–Ross,²⁸ Singwi–Sjolander,²⁹ has been proposed to quantify the QENS results. Parameters in these models are related to VHCF parameters by space Fourier transform. Due to the lack of QENS experimental results, we did not attempt to formulate a quantitative model for the “structured diffusion”.

Lithium distribution and its relation to phase transition

Probability density functions (p.d.f.) or density maps offer an intuitive way to visualize lithium distribution in the tetragonal and cubic phase. Fig. 6a shows the isosurface plot (isosurface level of 0.3 Å^{-3}) for a slice along the (111) lattice plane that constitute the looping structure of Li sites in the Li diffusion pathway, where the two tetrahedral sites (Td-8a and 16e) and two octahedral sites (Oh-32g and 16f) are all visible. Fig. 6a is

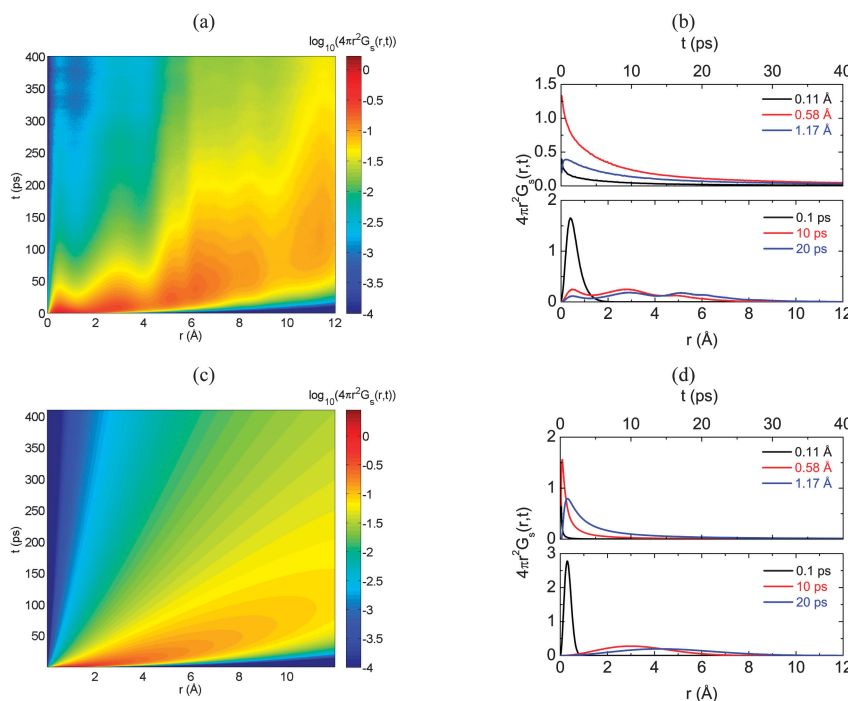


Fig. 5 (a) Self-part of the van Hove correlation function and (b) its spatial and temporal projection at 1100 K. (c) Self-part of the van Hove correlation function and (d) its spatial and temporal projection of a continuous random-walk model at 1100 K.

based on Rietveld refinement results so the density maps are local and harmonic (spheres or ellipsoids). Our 300 K MD simulation (Fig. 6b) predicts lithium density to be primarily located at the Td-8a, Oh-32g, and Oh-16f sites in agreement with Fig. 6a. However, we also observed a degree of anharmonicity arising from an elongation of the Oh-16f and Oh-32g sites toward the Td-16e sites. This elongation of the Oh-32g sites that connect Td-8a to Td-16e continues to grow as the temperature is increased, leading to a

small occupancy of the Td-16e site at 500 K (Fig. 6c). At 800 K (Fig. 6d) a near complete loop structure is observed for the tetragonal crystal. After the phase transition to cubic has occurred, the probability of occupying either of the now degenerate tetrahedral sites is equal, and a complete ring structure is observed as shown in the density map at 1100 K (Fig. 6e).

Additional insight into the phase transition can be obtained by examining the cage occupancy and MSD of lithium at

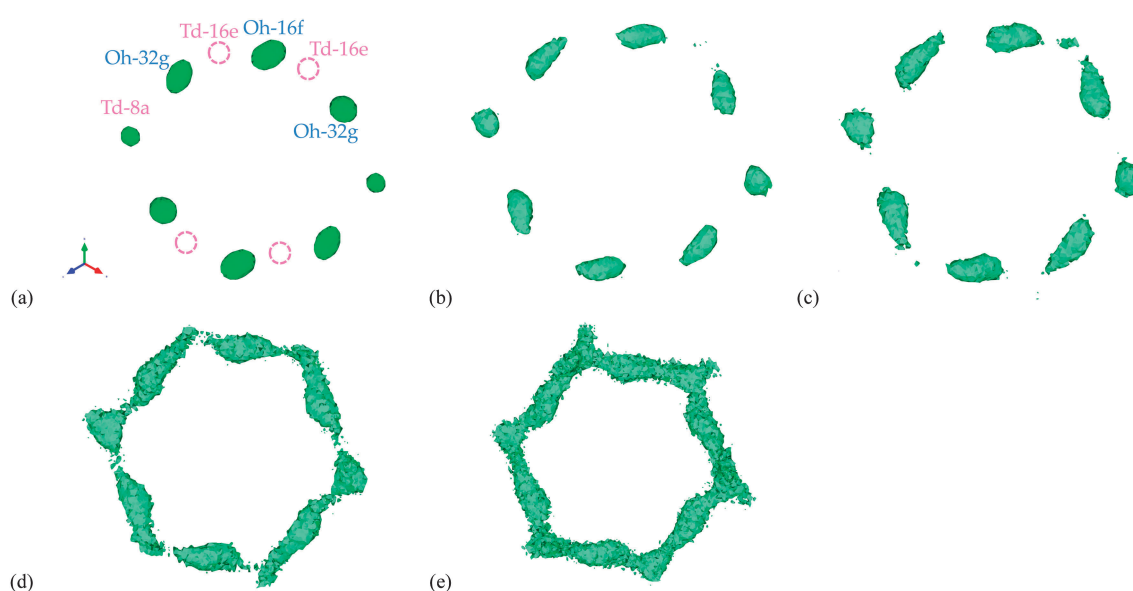


Fig. 6 Lithium density maps on (111) for Li₇LZ. (a) 300 K by Rietveld refinement, (b) 300 K, (c) 500 K, (d) 800 K, and (e) 1100 K by MD simulation. Isosurface level is 0.3 Å⁻³.

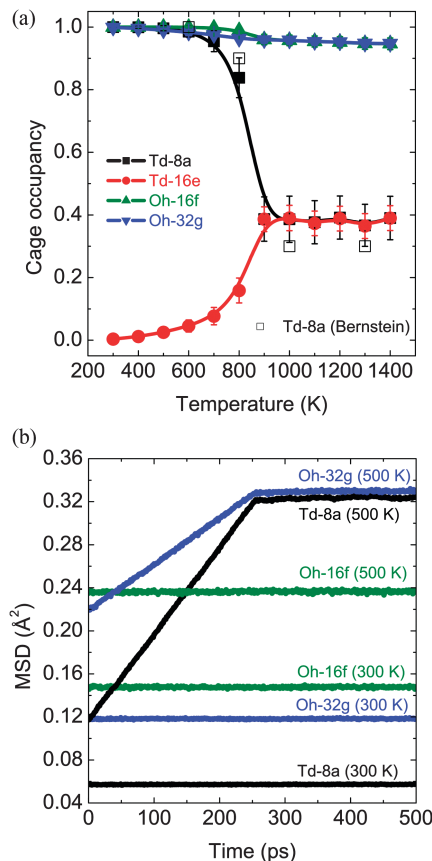


Fig. 7 (a) Occupancy of four different cages, including two tetrahedral (Td) and two octahedral (Oh), for lithium atoms as a function of temperature. Error bars represent the degree of dynamic fluctuation in the occupancy observed during MD simulation. Values from Bernstein *et al.*¹⁷ are shown for comparison. (b) Mean squared displacement of lithium at three different cages in the tetragonal phase at 300 and 500 K.

different sites shown in Fig. 7. The change in occupancies of tetrahedral sites with increasing temperatures (Fig. 7a) clearly indicates the depletion of Td-8a site and filling of Td-16e, especially around the transition temperature of 900 K. On the other hand, the occupancies of the two octahedral sites remain close to one at all temperatures, but do experience a decrease in occupancy as the temperature is increased. Equivalently, there is a small increase in the overall occupancy of the tetrahedral sites. The shift of lithium atoms from Td-8a to Td-16e site was also proposed by Bernstein *et al.*¹⁷ but they stated there was no exchange of lithium atoms between tetrahedral and octahedral sites. In the meantime, slightly lower Td occupancy was observed in their work, as shown in Fig. 7a. Error bars in this figure represent the degree of dynamic fluctuation in occupancy observed during MD simulation. Furthermore, the MSDs of all three sites at 300 K in Fig. 7b indicate lithium atoms oscillating as shown in the VHCF plot of Fig. 3. At 500 K, MSDs of Td-8a and Oh-32g lithium atoms show a simultaneous increase at short time suggesting that their motion is correlated.

From the above observation and discussion of both Fig. 6 and 7, we believe that the tetragonal to cubic phase transition is an entropy-driven one that involves redistribution of lithium

atoms among all tetrahedral sites. The ordered tetragonal structure is energetically favored as it has the smallest number of nearest-neighbor Li-Li repulsion pairs.¹ Redistribution of Li among all tetrahedral sites will increase the entropy but is likely to raise the internal energy, since an occupied Oh site (32g or 16f) has a maximum of only two Li-Li pairs while an occupied Td site (8a or 16e) has a maximum of four Li-Li pairs. Above the transition temperature, the entropy contribution overshadows the energy contribution. The transition is likely to initiate on the Td-8a site but needs the cooperation of neighboring Oh-32g sites. Lithium atoms at Oh-32g sites mainly act as relay atoms, instead of contributing directly to the filling of Td-16e site. Again, the reason that Oh sites prefer to be consistently occupied is to minimize Li-Li repulsion. However, there is indeed a slight shift of lithium atoms from octahedral to tetrahedral sites with increasing temperatures, since the higher temperature is more accommodating to increased Li-Li repulsion.

Lithium dynamics

We will now take a closer look at the structure of nearest-neighbor Li-Li pairs and their effects on lithium dynamics. There are theoretically 16 different ways in which lithium can distribute itself about neighboring Td and Oh sites, designated as clusters. A simplified notation has been previously introduced to easily differentiate the types of lithium clusters.¹⁵ First, the type of site is identified as either tetrahedrally (Txx) or octahedrally (Oxx) centered. The first 'x' is then used to identify a site as either occupied '1' or unoccupied '0'. The second 'x' in this notation refers to the number of nearest occupied lithium sites. For Txx this ranges from 0–4 because there are four Oh sites surrounding a Td site, and for Oxx this ranges from 0–2 with two neighboring Td sites.

Fig. 8 shows the evolution in the number of tetrahedrally and octahedrally centered clusters with temperature. The schematics of selected Txx and Oxx clusters are shown next to the plots. Pink squares and blue rectangles represent the tetrahedral and octahedral cages, respectively. For the low-temperature tetragonal phase at 300 K, there are only two types of observed clusters, T14 and T04 resulting from ordering about lithium sites, to minimize Li-Li repulsion. As we increase the temperature, the number of T14 and T04 clusters decreases, first leading to an increase in the originally unobserved T13 and eventually the creation of T03 clusters. A similar trend can be identified for the Oh clusters. Initially only O11 and O10 clusters are observed. As the temperature increases the amount of O10 remains relatively constant, but the concentration of O11 decreases significantly while we see the generation of the previously unobserved O12 and O02 clusters. It is to be noted that it was reported by Xie *et al.*³⁰ and Jalem *et al.*¹² that it was not possible to have O12 clusters in Li₇LZ, based on the exclusion principle. Error bars in Fig. 8 show the degree of fluctuation over the course of a simulation, with larger error bars signifying larger fluctuations from more mobile ions. The dominance of clusters with high coordination numbers, *e.g.* T_x3, T_x4, implies that highly correlated motion is expected, consistent with the low inverse thermodynamic factors throughout the

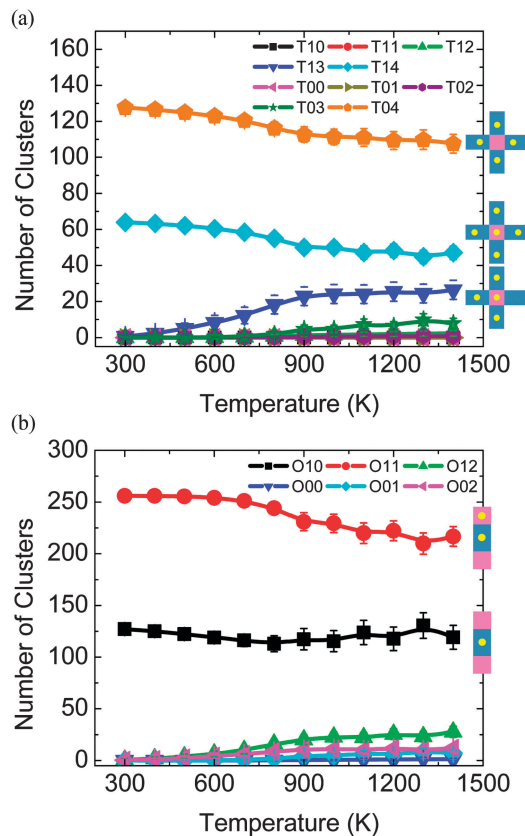


Fig. 8 Evolution of (a) tetrahedral centered clusters and (b) octahedral centered clusters. Schematics of some popular clusters were shown. Pink squares and blue rectangles represent the tetrahedral and octahedral cages, respectively. Yellow dots are lithium atoms. Error bars in the figures represent the degree of fluctuation in the number of clusters observed during MD simulation.

temperature range, and with lower inverse thermodynamic factors in the tetragonal phase as seen in Fig. 2d.

Finally, we try to visualize the oscillatory and diffusive motion discussed in Fig. 3 and 5. These results are shown in Fig. 9 and movies of these motions can be found in the ESI.† Fig. 9a and b show the schematics and trajectories (connected small beads) of vibratory motions exhibited by lithium atoms in T14 and T04 clusters at 300 K. Within a T14 cluster (Fig. 9a), the center is Td-8a site and four neighbors are Oh-32g sites. Lithium atoms at Oh-32g site are rattling around positions that are far away from the occupied Td-8a. Within a T04 cluster (Fig. 9b), the center is Td-16e site and two neighbors are Oh-32g and the other two are Oh-16f sites. Lithium atoms at Oh-32g and Oh-16f sites are rattling around but staying close to the empty 16e site. Both types of oscillation can be considered as ways to minimize Li-Li repulsion. Fig. 9c and d show the schematics and bottlenecks of diffusion in Li7LZ at 1100 K. In Fig. 9c, two lithium atoms (Li1 and Li2) will move in concert to change a T14 cluster to a T04 cluster. During the process, two triangular bottlenecks that connect the neighboring tetrahedral and octahedral cages were crossed. Locations of lithium atoms on these bottlenecks are also shown. The observation that lithium atoms prefer to stay close to one of the triangular edges

is referred to as an “edge-pass” mechanism. This mechanism has been suggested by the NEB study by Xu *et al.*,¹⁸ FPMD simulation by Jalem *et al.*¹² and Miara *et al.*,¹¹ and our classical MD simulation for Li5LT at low temperatures.¹⁵ Fig. 9d presents the correlated motion of three lithium atoms crossing four bottlenecks. First, both Li1 and Li2 move synchronously with Li1 expelling Li2 into the empty Td cage. Effectively this changes a T04 cluster to a T14 cluster. Then Li2 and Li3 move synchronously in that Li3 migrates into the empty Td cage on the left while Li2 hops into the Oh cage that hosted Li3 previously, reestablishing the T04 cluster. Examination of bottlenecks suggests that both “edge-pass” and “center-pass” mechanisms were observed.

To obtain statistical details on how lithium atoms move across the bottlenecks, we recorded the Li locations on the bottleneck for a simulation time between 900 ps to 1 ns in the MD simulation. More than 1000 lithium atoms were collected. As done in our recent work,¹⁵ we used both the distance to three corners, denoted as on-face-Li-to-oxygen distances, and distance to three edges, denoted as on-face-Li-to-edge distances, to project where lithium is relatively located as it diffuses through the bottleneck. Fig. 10a shows the distribution of these two distances at 1100 K. Gaussian distribution was observed for both distances; the most probable distances to the corner and to the edge are around 1.8 Å and 0.8 Å, respectively. Such distribution suggests that the majority of Li⁺ pass through the center of bottleneck as shown in Fig. 10c, while the “edge-pass” type, corresponding to the tails in the distribution, is a minority mechanism. Even at the lower temperature of 600 K in the tetragonal phase, Fig. 10b, the distribution can still be approximated as a Gaussian, although a shoulder peak appears at around 1.2 Å in the bottom plot. Such “center-pass” mechanism for a wide temperature range in Li7LZ is in contrast to the scenario in Li5LT, in which “center-pass” and “edge-pass” mechanisms dominate at high temperature (e.g. above 1100 K) and low temperature (e.g. 550 K, 700 K), respectively.¹⁵

The deterministic factors of “center-pass” and “edge-pass” mechanism can be understood from the consideration of global and local symmetry. It is expected that the centers of a tetrahedron and of a bottleneck would be favored for Li to pass from the perspective of global symmetry, while local symmetry might distort this picture, especially at lower temperatures. In Fig. 8 we saw that T04 dominates the T0x clusters in Li7LZ. It can be reasoned that the local symmetry of T04 clusters causes a more uniform repulsive force on the Li, making the center of the bottleneck the easiest for the Li to approach. In Li5LT there was a greater variety of clusters observed especially at low temperature.¹⁵ These clusters have a greater local asymmetry at most tetrahedrons due to Li⁺ not fully occupying the surrounding octahedral sites, causing an asymmetrical force to be applied to Li and push it to the edge of the bottleneck. At higher temperatures, the influence of local Li-Li repulsion becomes less important and Li will proceed with a “center-pass” pattern in either material consistent with the global symmetry.

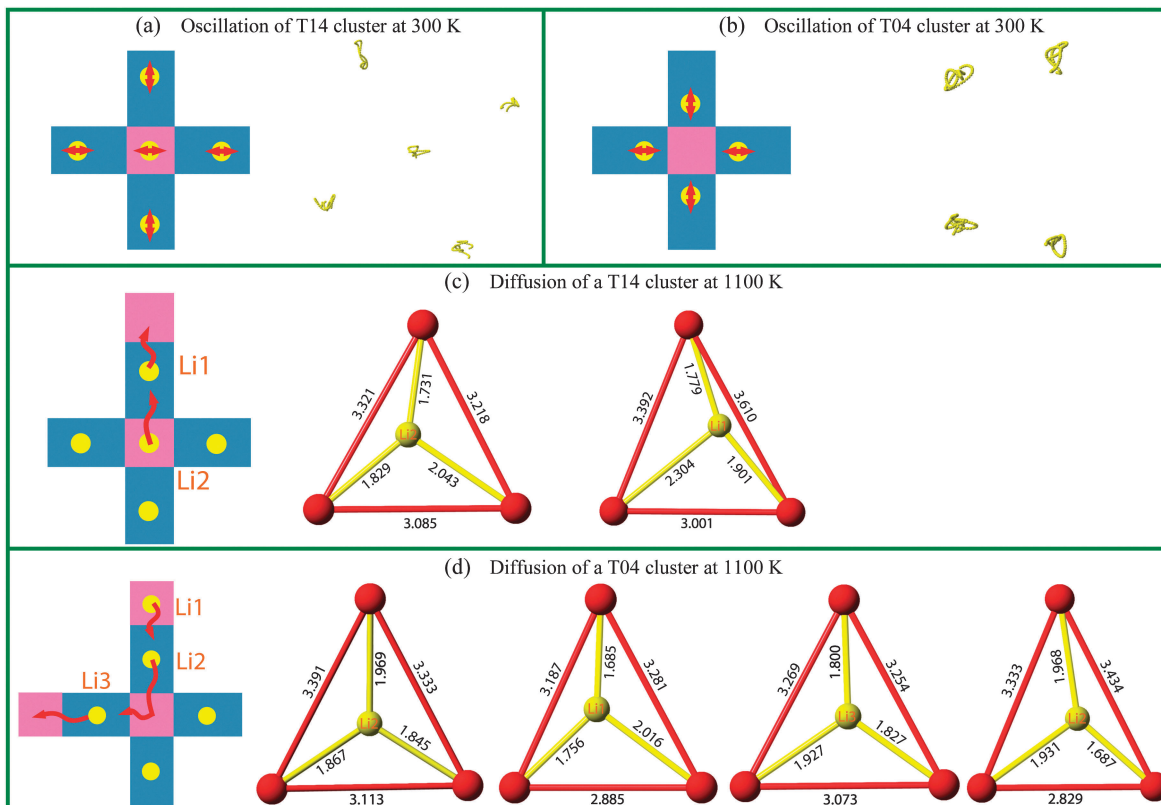


Fig. 9 Examples of lithium dynamics at 300 K for (a) a T14 cluster, (b) a T04 cluster, and at 1100 K for (c) a T14 cluster, (d) a T04 cluster. Yellow dots represent Li atoms. Pink squares and blue rectangles schematically represent Td and Oh cages, respectively. Red circles represent oxygen atoms on the triangles (bottlenecks). Distances (in Å) between O–O and Li–O atoms are labeled to illustrate the geometry of the bottleneck and lithium location as lithium goes this triangular face.

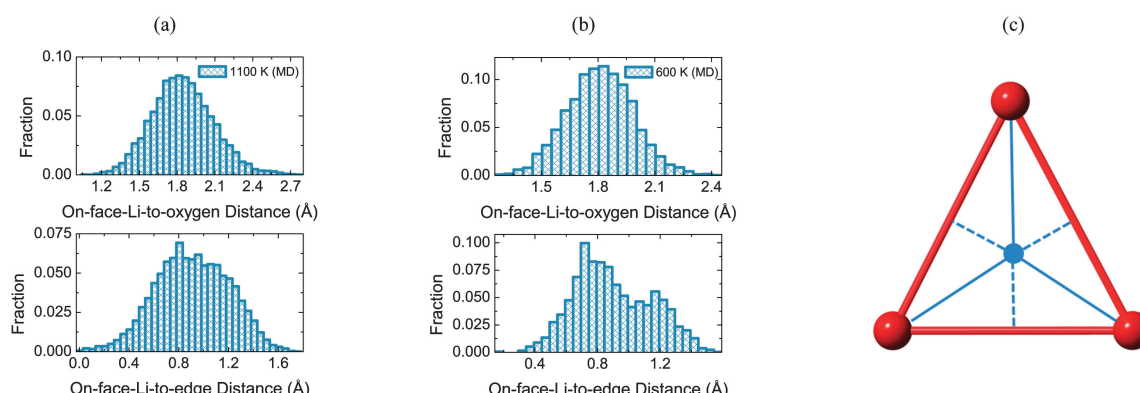


Fig. 10 Distribution of displacements of lithium to bottleneck oxygen atoms and edges, i.e. on-face-Li-to-oxygen and on-face-Li-to-edge distances, at (a) 1100 K as a cubic phase and (b) 600 K as a tetragonal phase. (c) Schematics of the two distances and “center-pass” location.

Conclusions

Using molecular dynamics, we investigated local structure and dynamics in the solid electrolyte $\text{Li}_7\text{La}_3\text{Zr}_2\text{O}_{12}$ and origin of tetragonal to cubic phase transition. First, validation of our force-field parameters was accomplished by comparing our simulation output to lattice parameter, neutron scattering, and conductivity measurements obtained from experimental techniques. Thermal expansion, phase transition, and neutron

scattering PDF, and conductivity results at various temperatures concur with experimental values. Second, we show that lithium dynamics predominantly consisted of oscillations at low temperatures in the tetragonal phase and “structured diffusion” in the high temperature cubic phase. This was accomplished by combining self and distinct part of van Hove correlation function and MSD data to make a more complete analysis of structure and dynamics of Li. Third, we show that the tetragonal to cubic phase transition coincides with the

redistribution of Td-8a lithium to Td-16e sites. For this reason, we believe that the phase transition from tetragonal to cubic is entropy driven. Li diffusion is likely initiated at the 8a tetrahedral sites, requiring the neighboring 32g octahedral lithium to simultaneously diffuse into the unoccupied 16e tetrahedral site. However, lithium at 32g site mainly act as relay atoms and only contribute slightly to the direct filling of 16e site at high temperatures. Finally, we see that in both the tetragonal and cubic phase that lithium is locally distributed in clusters in only a few ways. These local clusters are mostly symmetrical leading to a “center-pass” mechanism dominating most of the diffusion through the bottleneck.

Appendix

Static and dynamic structure functions: number density function

The dynamics of a multi-component material with n different chemical species can be described by a total number of n number density functions $\rho_i(\mathbf{r}, t) = \sum_{k=1}^{N_i} \delta[\mathbf{r} - \mathbf{r}_{i,k}(t)]$, where \mathbf{r} is an arbitrary position in the material, $\mathbf{r}_{i,k}(t)$ is the position of k th atom of species i at time t , and N_i is the total number of atoms in species i . The time-averaged number density function $\rho_i(\mathbf{r}_l) = \langle \rho_i(\mathbf{r}_l, t) \rangle_t$ over all pixels (at location \mathbf{r}_l) in the simulation cell yields the probability density function (p.d.f.) or density map of each species as shown in Fig. 6.

Static and dynamic structure functions: van Hove correlation function

Another standard function characterizing dynamics of materials is the van Hove time-space correlation function²⁶ of species i that describes the correlation of number density as the following:

$$G_{ii}(\Delta\mathbf{r}, \Delta t) = \frac{1}{N_i} \left\langle \sum_{k=1}^{N_i} \sum_{l=1}^{N_i} \delta[\Delta\mathbf{r} + \mathbf{r}_{i,k}(0) - \mathbf{r}_{i,l}(\Delta t)] \right\rangle \quad (\text{A1})$$

This function can be separated as a “self” part $G_{ii,s}(\mathbf{r}, t)$ and a “distinct” part $G_{ii,d}(\Delta\mathbf{r}, \Delta t)$ as the following:

$$\begin{aligned} G_{ii,s}(\Delta\mathbf{r}, \Delta t) &= \frac{1}{N_i} \left\langle \sum_{k=1}^{N_i} \delta[\Delta\mathbf{r} + \mathbf{r}_{i,k}(0) - \mathbf{r}_{i,k}(\Delta t)] \right\rangle, \\ G_{ii,d}(\Delta\mathbf{r}, \Delta t) &= \frac{1}{N_i} \left\langle \sum_{k=1}^{N_i} \sum_{l \neq k}^{N_i} \delta[\Delta\mathbf{r} + \mathbf{r}_{i,k}(0) - \mathbf{r}_{i,l}(\Delta t)] \right\rangle \end{aligned} \quad (\text{A2})$$

$G_{ii,s}(\Delta\mathbf{r}, \Delta t)$ or its transformed version $4\pi r^2 G_{ii,s}(\Delta\mathbf{r}, \Delta t)$, is related to the probability of finding one atom after it travels a vector distance of $\Delta\mathbf{r}$ for a time interval of Δt . On the other hand, distinct-part of van Hove correlation function, $G_{ii,d}(\Delta\mathbf{r}, \Delta t)$ or its transformed version $4\pi r^2 G_{ii,d}(\Delta\mathbf{r}, \Delta t)$, is related to the probability of finding one atom when a different atom is away from this atom with a vector distance of $\Delta\mathbf{r}$ and a time interval of Δt . For isotropic materials, the vector $\Delta\mathbf{r}$ is reduced to a scalar Δr .

The “static” ($\Delta t = 0$) version of $G_{ii}(\Delta\mathbf{r}, \Delta t)$ can be written as the following:

$$G_{ii}(\Delta\mathbf{r}, 0) = \delta(\Delta r) + \rho_i g_{ii}(\Delta r) \quad (\text{A3})$$

where $g_{ii}(r)$ is the “static” atomic pair distribution function and $\rho_i = N_i/V$ is the average number density. Due to this ρ_i term, it can be convenient to divide $G_{ii,d}(\Delta r, \Delta t)$ by ρ_i to obtain a normalization, which is the form used in the present paper. In addition, mean square displacement $\langle \Delta r_i(t) \rangle^2$ is related to the self-part of van Hove correlation function as:

$$\langle \Delta r_i(t) \rangle^2 = \int_0^\infty (\Delta r)^2 \cdot 4\pi(\Delta r)^2 G_{ii,s}(\Delta r, \Delta t) d\Delta r \quad (\text{A4})$$

For the oscillation-type dynamics, $G_{ii,s}(\Delta r, \Delta t)$ and $\langle \Delta r_i(t) \rangle^2$ can be approximated as

$$\begin{aligned} 4\pi(\Delta r)^2 G_{ii,s}(\Delta r, \Delta t) &= 4\pi(\Delta r)^2 \frac{1}{(\pi u_i^2)^{3/2}} \exp\left[-\frac{(\Delta r)^2}{u_i^2}\right], \\ \langle \Delta r_i(t) \rangle^2 &= \frac{3}{2} u_i^2 \end{aligned} \quad (\text{A5})$$

where u_i^2 is a parameter of average displacement. For the continuous random-walk type diffusion, $G_{ii,s}(\Delta r, \Delta t)$ and $\langle \Delta r_i(t) \rangle^2$ can be approximated as

$$\begin{aligned} 4\pi(\Delta r)^2 G_{ii,s}(\Delta r, \Delta t) &= 4\pi(\Delta r)^2 \frac{1}{(4\pi D \Delta t)^{3/2}} \exp\left[-\frac{(\Delta r)^2}{4D\Delta t}\right], \\ \langle \Delta r_i(t) \rangle^2 &= 6D\Delta t \end{aligned} \quad (\text{A6})$$

For simplicity, we will use r and t instead of Δr and Δt in van Hove correlation functions in the main text. The extension of all functions above to other pairs of species i and j ($i \neq j$) and their relation to experimental double differential cross section from neutron scattering can be found in the references.^{31–35}

Acknowledgements

We wish to acknowledge the Michigan State University High Performance Computing Center and the Institute for Cyber-Enabled Research for access to their computing resources. We acknowledge the financial support by the Ceramics Program of National Science Foundation (DMR-1206356).

Notes and references

- Y. X. Wang, A. Huq and W. Lai, *Solid State Ionics*, 2014, **255**, 39–49.
- J. Awaka, N. Kijima, H. Hayakawa and J. Akimoto, *J. Solid State Chem.*, 2009, **182**, 2046–2052.
- G. Larraz, A. Orera and M. L. Sanjuan, *J. Mater. Chem. A*, 2013, **1**, 11419–11428.
- J. M. Tarascon and M. Armand, *Nature*, 2001, **414**, 359–367.
- M. Armand and J. M. Tarascon, *Nature*, 2008, **451**, 652–657.
- J. B. Goodenough and Y. Kim, *Chem. Mater.*, 2010, **22**, 587–603.
- V. Thangadurai, S. Narayanan and D. Pinzar, *Chem. Soc. Rev.*, 2014, **43**, 4714–4727.
- M. Matsui, K. Takahashi, K. Sakamoto, A. Hirano, Y. Takeda, O. Yamamoto and N. Imanishi, *Dalton Trans.*, 2014, **43**, 1019–1024.

- 9 E. J. Cussen, *J. Mater. Chem.*, 2010, **20**, 5167–5173.
- 10 Y. Wang and W. Lai, *J. Power Sources*, 2015, **275**, 612–620.
- 11 L. J. Miara, S. P. Ong, Y. F. Mo, W. D. Richards, Y. Park, J. M. Lee, H. S. Lee and G. Ceder, *Chem. Mater.*, 2013, **25**, 3048–3055.
- 12 R. Jalem, Y. Yamamoto, H. Shiiba, M. Nakayama, H. Munakata, T. Kasuga and K. Kanamura, *Chem. Mater.*, 2013, **25**, 425–430.
- 13 S. Adams and R. P. Rao, *J. Mater. Chem.*, 2012, **22**, 1426–1434.
- 14 C. A. Geiger, E. Alekseev, B. Lazic, M. Fisch, T. Armbruster, R. Langner, M. Fechtelkord, N. Kim, T. Pettke and W. Weppner, *Inorg. Chem.*, 2011, **50**, 1089–1097.
- 15 Y. X. Wang, M. Klenk, K. Page and W. Lai, *Chem. Mater.*, 2014, **26**, 5613–5624.
- 16 A. Kuhn, S. Narayanan, L. Spencer, G. Goward, V. Thangadurai and M. Wilkening, *Phys. Rev. B: Condens. Matter Mater. Phys.*, 2011, **83**, 094302.
- 17 N. Bernstein, M. D. Johannes and K. Hoang, *Phys. Rev. Lett.*, 2012, **109**, 205702.
- 18 M. Xu, M. S. Park, J. M. Lee, T. Y. Kim, Y. S. Park and E. Ma, *Phys. Rev. B: Condens. Matter Mater. Phys.*, 2012, **85**, 052301.
- 19 T. L. Katharina Meier and A. Curioni, *J. Phys. Chem. C*, 2014, **118**, 6668–6679.
- 20 W. Smith and T. R. Forester, *J. Mol. Graphics*, 1996, **14**, 136–141.
- 21 P. J. Mitchell and D. Fincham, *J. Phys.: Condens. Matter*, 1993, **5**, 1031–1038.
- 22 S. K. Schnell, X. Liu, J. M. Simon, A. Bardow, D. Bedeaux, T. J. H. Vlugt and S. Kjelstrup, *J. Phys. Chem. B*, 2011, **115**, 10911–10918.
- 23 C. L. Farrow, P. Juhas, J. W. Liu, D. Bryndin, E. S. Bozin, J. Bloch, T. Proffen and S. J. L. Billinge, *J. Phys.: Condens. Matter*, 2007, **19**, 335219.
- 24 C. E. Mohn, S. Stolen, S. T. Norberg and S. Hull, *Phys. Rev. Lett.*, 2009, **102**, 4.
- 25 D. A. Keen, *J. Phys.: Condens. Matter*, 2002, **14**, R819–R857.
- 26 L. Vanhove, *Phys. Rev.*, 1954, **95**, 249–262.
- 27 C. T. Chudley and R. J. Elliott, *Proc. Phys. Soc., London*, 1961, **77**, 353.
- 28 P. L. Hall and D. K. Ross, *Mol. Phys.*, 1981, **42**, 673–682.
- 29 K. S. Singwi and A. Sjolander, *Phys. Rev.*, 1960, **119**, 863–871.
- 30 H. Xie, J. A. Alonso, Y. T. Li, M. T. Fernandez-Diaz and J. B. Goodenough, *Chem. Mater.*, 2011, **23**, 3587–3589.
- 31 N. W. Ashcroft and D. C. Langreth, *Phys. Rev.*, 1967, **156**, 685.
- 32 T. E. Faber and J. M. Ziman, *Philos. Mag.*, 1965, **11**, 153.
- 33 S. W. Lovesey, *Theory of Neutron Scattering from Condensed Matter*, Oxford University Press, 1984.
- 34 D. A. Keen, *J. Appl. Crystallogr.*, 2001, **34**, 172–177.
- 35 T. Egami and S. J. L. Billinge, *Underneath the Bragg Peaks: Structural Analysis of Complex Materials*, 2nd edn, 2012.